Renewable Energy 178 (2021) 96–107

Contents lists available at ScienceDirect

Renewable Energy

journal homepage: www.elsevier.com/locate/renene

Biogenic architectures for green, cheap, and efficient thermal energy storage and management

Mattia Biesuz *, Francesco Valentini , Mauro Bortolotti , Andrea Zambotti , Francesca Cestari , Angela Bruni , Vincenzo M. Sglavo , Gian D. Sorarù , Andrea Dorigato , Alessandro Pegoretti

University of Trento, Department of Industrial Engineering, Via Sommarive 9, 38123, Trento, Italy

ARTICLE INFO

Article history:
Received 4 January 2021
Received in revised form
29 May 2021
Accepted 14 June 2021
Available online 16 June 2021

Keywords:
Thermal energy storage
Porous materials
Phase change materials
Shape stabilization
Biogenic materials

ABSTRACT

A key challenge for efficient thermal management of civil buildings is the development of shape-stabilized phase change materials (PCM) for thermal energy storage and release. Nevertheless, some issues related to the disposal of such devices are arising as they are generally not biodegradable and recyclable. In this work, we developed two new renewable and biodegradable thermal energy storage composites obtained from renewable resources. These are based on the use of bio-derived alcohol as PCM and on porous biogenic structures, namely cuttlebone and pomelo peel, as shape stabilizers, which are currently waste materials. The results point out that both cuttlebone and pomelo peel can spontaneously absorb huge amounts of the considered PCM and retain it in the liquid state. The thermal energy storage capacity of the composites is about 70% that of neat PCM, whereas the volumetric efficiency (i.e., the ratio between the thermal energy storage capacity of the composite and the neat PCM in J cm^{-3}) approaches 90% and 70% in cuttlebone and pomelo peel composites, respectively. The properties appear stable over at least 100 melting/solidification cycles.

1. Introduction

Nowadays, the awareness of the environmental problems related to global warming [1] is driving the research to more efficient thermal energy management [2]. In this context, recent environmental regulations have opened ambitious challenges for researchers. For instance, the European Union (EU) targeted for the year 2030 a 40% reduction of greenhouse gas emissions compared to 1990 [3]. Efficient management of thermal energy in civil buildings is a key tool to achieve such goal; in fact, in 2017 more than 600 Mt of CO_2 equivalent greenhouse gasses were produced by households on the EU level, much more than industry (≈ 400 Mt) and agriculture (≈ 400 Mt) [3].

Among the different strategies suitable to increase the energy efficiency of civil buildings, thermal energy storage (TES) is one of the most promising [4–7]. Here, the seasonal or daily excess of thermal energy (accumulated during the hottest hours or seasons) is stored in specific devices and released as the environmental temperature decreases. In other words, TES aims at increasing the thermal inertia of the building, thus resulting in a substantial stabilization of its temperature and reducing the energy demand and CO_2 footprint of the heating or cooling systems. To store such a large amount of thermal energy (without significantly impacting on the total mass or volume of the building) materials with high thermal energy storage capacity per unit weight or volume are needed. Since crystallization/melting phase transitions allow to release/absorb a large amount of heat (latent heat), materials with a melting point around 20 °C are of particular interest [5,8–10]. These phase change materials (PCM) are usually organic compounds including paraffin waxes [5,8,9], polyethylene glycol [11], and other oil-derived compounds. However, paraffin is not renewable and biodegradable and one can foresee that extensive use of paraffin in civil TES devices could open additional issues related to their end-of-life and waste disposal. On the other hand, new biodegradable, green, and renewable PCMs are currently emerging, and among them, fatty acids and alcohols are particularly relevant [12–20].

For practical use of PCMs in TES devices, the materials need to be shape-stabilized to avoid their leakage in the molten state. This can be achieved either by encapsulation [4,8,18–21] or shape

* Corresponding author.
E-mail address: mattia.biesuz@unitn.it (M. Biesuz).

https://doi.org/10.1016/j.renene.2021.06.068
0960-1481/

stabilization [8,22–26], using porous structures able to absorb and contain molten PCM. Both synthetic polymeric (i.e., polyethylene [27], polypropylene [28], polyurethane [29,30], and others [31]) and inorganic matrices have been shown to act as efficient shape stabilizers. Nevertheless, synthetic organic matrices present several issues regarding their end-of-life. This is especially true if one considers that they are not pure substances but composites containing PCM at the micro- or even nano-scale, this making traditional recycling procedures unsuitable. On the other hand, inorganic matrices (i.e., mesoporous SiO_2 [22,32–34], porous graphite [35,36], carbon nanomaterials [6,22,37,38], silica fume [39,40], diatomite [12,15,41–43], porous alumina [38], nanofibrous ceramics [44], expanded perlite and vermiculite [13] …) might require a sophisticated and expensive synthesis or high temperature treatments (pre-sintering) to attain porous but mechanically consistent architectures.

In this context, the research of new shape stabilizers remains a key challenge. Despite the development of synthetic procedures to highly porous materials is an intriguing research topic, we can observe that living beings in Nature continuously and spontaneously produce large amounts of porous microstructures [45–47] including both organic (i.e., wools, pelts, sponges …) and inorganic (i.e., porous bones, skeletal …) compounds. Moreover, most of them are substantially available "for free" as they are considered wastes. The availability of cheap and renewable shape stabilizers is a fundamental aspect for a shift toward smart buildings with improved thermal energy management: extensive employment of TES in civil structures would require huge amounts of shape stabilizers, whose cost is expected to have a significant economic impact.

The present work aims to develop new environmentally friendly composites for TES applications, where the PCM is a commercially available agriculture-derived biodegradable alcohol and the shape stabilizer is a natural porous structure. Two specific shape stabilizers are investigated for the first time, cuttlebone and pomelo peel. Pomelo is a fruit belonging to the *citrus* family mostly diffuse in China and South-East Asia. Its world production currently approaches 10 Mt/year and constantly grew over the past decade [48]. It possesses a thick peel mostly constituted by a porous *albedo* (the spongy white part of *citrus* fruits peel). Cuttlefish is a *cephalopod*, whose world production was about 3.6 Mt/year in 2010 [49]. It contains a porous carbonaceous bone (cuttlebone) which is used as a buoyancy tank. Cuttlefish maintain their vertical position underwater by regulating the amount of water inside their bone.

The *rationale* behind the choice of the shape stabilizers is the following: (i) both are highly porous and of biogenic origin; (ii) they do not contain dangerous substances and they are "renewable"; (iii) the waste disposal is easy since pomelo peel can be fully biodegraded, whereas cuttlebone can be easily milled to produce carbonaceous sand; (iv) one is organic whereas the other is inorganic; and (v) both are considered wastes and are extremely diffuse. Therefore, their application in TES devices has the double advantage of using a cheap and easily available shape stabilizer while providing a new life and function to waste materials.

2. Experimental procedures

2.1. Raw materials and samples preparation

Commercially-available pomelo and cuttlefish were purchased in a supermarket in Trento (Italy). The pomelo peel was dried in an oven at 180 °C for 30 min to remove any residual absorbed water and sterilize it. Cuttlebone samples were boiled in distilled water for 10 min and then dried at 100 °C for 24 h. The samples were cut with a diamond saw. Pomelo peel samples were shaped into parallelepipeds with sizes of about 1x1x0.7 cm^3. The cuttlebone was cut into slices orthogonally to its main axis, each slice thickness being approximately 5 mm. Each portion was then divided into two parts, thus obtaining two samples per slice.

The pomelo peel and the cuttlebone samples were used to absorb the phase change material (PCM). For this purpose, PureTemp®23 was selected and acquired by Octochem Inc (Vadalia, USA). It is characterized by a melting point of 23 °C, a density of 0.83 g cm^{-3} at the liquid state, and a melting enthalpy (ΔH_m) of 227 J g^{-1}. PureTemp® 23 is derived from agricultural sources (certified from the United States Department of Agriculture), it is non-toxic and certified biodegradable. This PCM was selected to store/release thermal energy near room temperature conditions. The PCM absorption was performed by direct immersion of the samples within the liquid PureTemp® 23, on a heated plate at 40 °C, and it occurred within 5 min. Excess of PCM was used during the impregnation tests, the volume of the liquid PCM being about three times that of the shape stabilizer. Impregnation was carried out in atmospheric conditions (i.e., no vacuum infiltration).

2.2. Characterization of the constituents

The Fourier transform infrared spectra (FTIR) were acquired in attenuated total reflectance (ATR) mode using a Perkin Elmer FT-IR Spectrometer (Perkin-Elmer, USA) in a wavenumber range of 4000–650 cm^{-1}. Four scans with a resolution of 4 cm^{-1} were performed.

The pomelo peel microstructure was investigated by SEM (JSM-IT300LV) operating in low vacuum conditions. The morphology of the powders was investigated by field emission scanning electron microscopy, using an FE-SEM SUPRA 40 (Carl Zeiss Microscopy GmbH) instrument. The initial porosity of the matrices was estimated by comparing the skeletal density, measured using a gas displacement AccuPycII 1330 pycnometer (Micrometrics Instrument Corporation, USA), and the bulk density, measured by geometrical method. Hg porosimetry was employed to investigate the pore size distribution of the cuttlebone (the analysis was not possible on pomelo peel as it resulted compressible during the test). The analysis was carried out using a Porosimeter 2000 (Carlo Erba, Milano, Italy) facility, in the 0.2–2000 bar pressure range at 20 °C.

XRD spectra were recorded on an Italstructures IPD3000 diffractometer equipped with a Co anode source (line focus) coupled to a multilayer monochromator to select the K-α characteristic radiation (1.7889 Å) and fixed 100 μm slits. The porous matrix bulk samples, as well as the pure PCM and composites, were mounted on standard aluminum back-loading supports and measured in reflection geometry with a fixed 5° incidence angle. In the case of pure PCM and composite samples, a liquid nitrogen bath was set up directly below the sample holder to avoid melting due to X-Ray exposure. Diffraction patterns were then collected through an Inel CPS120 detector over the 5–120° 2θ range (0.03° per channel) with an acquisition time of 10 min for each sample.

2.3. Characterization of the composites

A leaking test was performed to verify the ability of the different materials to retain the PCM. The specimens were placed in an oven, at 40 °C, on different substrates (earthenware and porphyry bricks, absorbent paper, and aluminum foil) and their mass was monitored for 14 days to determine the PCM leakage. The samples were placed in contact with the substrates in two different modes: (i) the porous-spongy part of the shape stabilizer in contact with the substrate; (ii) the contact was localized on the dense outer shell of the composite matrix. The composites were further characterized

by FT-IR and XRD using the same procedures described in section *2.2*; their microstructure was investigated with a digital optical microscope Olympus DSX1000 operating in dark field mode and "fine" Z-axis scan.

Differential scanning calorimetry (DSC) measurements were carried out on the prepared samples (after the 14-days leaking test) using a Mettler DSC30 calorimeter under a nitrogen flow (10 cm^3 min^{-1}). A heating scan from −30 °C to 70 °C was followed by a cooling stage from 70 °C to −30 °C. All the thermal ramps were carried out at 10 °C min^{-1}. In this way, the onset point of the melting and crystallization peak ($T_{on,m}$, $T_{on,c}$), the melting and crystallization peak temperatures (T_m, T_c), and the specific melting and crystallization enthalpy values ($\Delta H_{wt,m}$, $\Delta H_{wt,c}$) were obtained. The volumetric specific enthalpy ($\Delta H_{vol,m}$, $\Delta H_{vol,c}$) was evaluated by multiplying the experimental enthalpy values by the density of each composite sample (ρ). The density of each material was estimated from the density of the PCM (0.83 g cm^{-3} at the liquid state), the initial porosity and skeletal density of the shape stabilizers, and the amount of PCM in the composite.

Moreover, the thermal energy storage efficiency was determined upon heating ($\eta_{wt,m}$) and the cooling ($\eta_{wt,c}$) scans as the ratio between the specific enthalpy of the sample and the corresponding specific enthalpy of neat PCM, as given in Equations (1), (2):

$$\eta_{wt,m} = \left(\frac{\Delta H_{wt,m}}{\Delta H_{wt,mPCM}}\right)100 \quad (1)$$

$$\eta_{wt,c} = \left(\frac{\Delta H_{wt,c}}{\Delta H_{wt,cPCM}}\right)100 \quad (2)$$

where $\Delta H_{wt,mPCM,}$ and $\Delta H_{wt,cPCM}$ are the specific enthalpies associated with melting and crystallization of the neat PCM, respectively.

The volumetric thermal energy storage efficiency was determined upon heating ($\eta_{vol,m}$) and cooling ($\eta_{vol,c}$) scans as the ratio between the volumetric specific enthalpy of the samples and the corresponding volumetric specific enthalpy of neat PCM, as given in Equations (3), (4):

$$\eta_{vol,m} = \left(\frac{\Delta H_{vol,m}}{\Delta H_{vol,mPCM}}\right)100 \quad (3)$$

$$\eta_{vol,c} = \left(\frac{\Delta H_{vol,c}}{\Delta H_{vol,cPCM}}\right)100 \quad (4)$$

where $\Delta H_{vol,mPCM,}$ and $\Delta H_{vol,cPCM}$ are the specific enthalpy associated with melting and crystallization of the neat PCM, respectively.

Furthermore, DSC was repeated after 20, 60, and 100 melting/solidification cycles to verify the stability of the thermal energy storage properties. The cyclic DSC measures were carried out on the same samples used for the 14-days leakage test. Only the samples contacting absorbent paper on their external shell were investigated. The cyclic solidification/melting process was carried out by soaking the < 100 mg of composite in a fridge at −15 °C and an oven at 80 °C for 5 min.

The overall thermal performance of the materials (after the 14-days leaking test) was investigated recording their surface temperature using an infrared thermal imaging camera FLIR E60 (emissivity = 0.86). The specimens were heated in an oven at 40 °C overnight and then inserted in a fridge kept at a temperature of 5 °C. In the same way, the specimens were cooled at −15 °C overnight and then inserted in an oven at 40 °C.

3. Results and discussion

3.1. Characterization of the constituents

The FTIR spectra of the raw materials used in the present work are reported in Fig. 1. All IR absorption peaks of cuttlebone (CB) can be related to the vibrational modes of the inorganic skeleton CO_3^{2-} groups [50]. The peaks well match those of calcium carbonate: in particular, the peaks at 1082 cm^{-1} and 853 cm^{-1} are typical of aragonite [51]. The aragonitic nature of cuttlebone is also confirmed by XRD (Fig. 2), clearly indicating orthorhombic symmetry with the two main (1 1 1) and (0 2 1) reflections located at $2\theta = 30.85°$ and 32.03° respectively [52]; from a microstructural point of view, average volume-weighted crystallite size of pure aragonite resulted about 36 nm.

The FTIR spectrum of pomelo peel (PP) is more complicated because of the presence of multiple organic components [53–60]. According to the scientific literature, its skeleton contains pectin (forming the largest part of the cell walls), cellulose, hemicellulose, and lignin [55–57]. These are mixed with other low-molecular-weight proteins, fats, soluble sugar, ashes, and volatile compounds (olefin, flavonoids …) [54,55,58]. The PP spectra in Fig. 1 well match those reported in previous works [53,59,60]. The broad absorption band at ≈ 3300 cm^{-1} can be assigned to the vibrations of the −OH groups of pectin, cellulose, hemicellulose, lignin, and flavonoids. The band at 2913 cm^{-1} can be attributed to the stretching of C–H bonds of sp^3 carbon. The feature at 1730 cm^{-1} is due to the C=O vibrations of the $-COOCH_3$ esters in pectin. The peak at ≈ 1600 cm^{-1} is likely related to the O–H bending of adsorbed water. The feature at 1368 cm^{-1} can be assigned to C–H bending; at 1234 and 1151 cm^{-1} the absorption bands of the C–O vibrations are visible. The broad asymmetric band with a minimum at 1012 cm^{-1} is probably due to the superposition of different absorption peaks including the C–O bending and the C–O–C

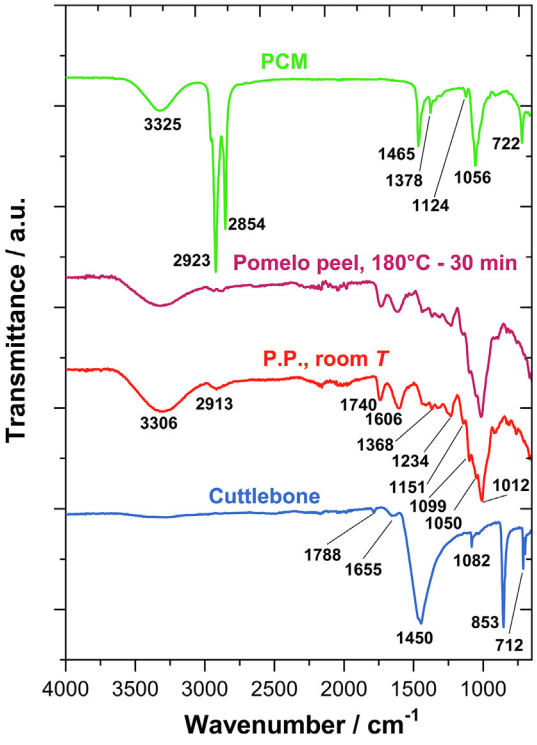

Fig. 1. FTIR spectra collected in ATR mode of the shape stabilizers (cuttlebone and pomelo peel) and of the used PCM (PureTemp 23®).

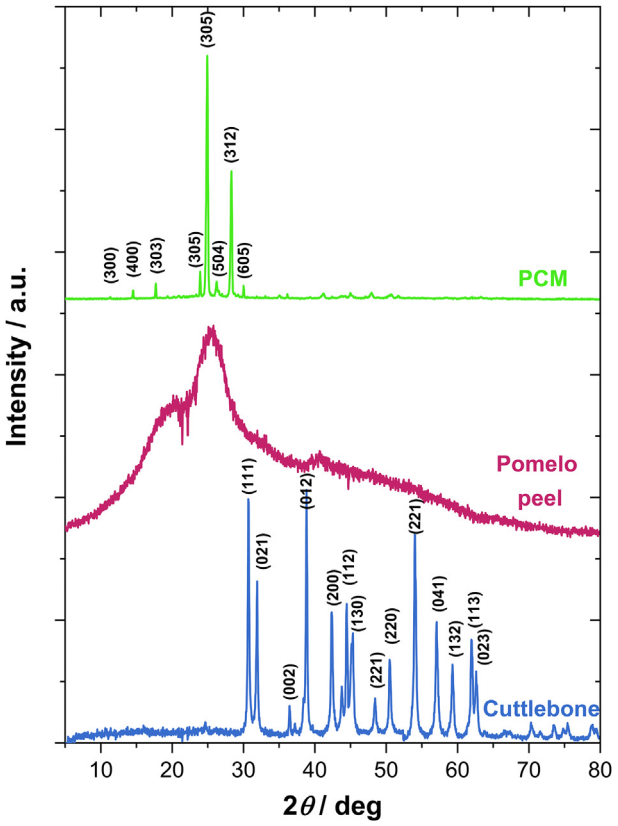

Fig. 2. XRD pattern of the shape stabilizers (cuttlebone and pomelo peel) and of the used PCM (PureTemp 23®). The main aragonite peaks are indexed in the CB spectrum, the peaks indexed in the PCM spectrum correpond to the monoclinic lattice described in the text.

skeletal vibrations of the pyranose rings. No substantial modification of the FTIR spectrum can be observed after the drying of PP at 180 °C. The PP has a nanocrystalline nature as shown in Fig. 2, with the XRD pattern exhibiting broad diffuse signals arising from short order periodicity, located in particular at $2\theta = 19.5°$ and 25.5° (5.47 Å and 4.6 Å interplanar distance respectively). In the absence of a structural model, no accurate structural and microstructural characterization can be performed; however, assuming an isotropic crystallite shape and the absence of lattice strain, the average volume-weighted crystallite size can be estimated around 10 Å using the classical Williamson-Hall approximation [61].

FTIR spectrum of PCM (PureTemp® 23) points out that it is saturated alcohol. The vibrations of −OH alcoholic groups are visible at ≈ 3325 cm^{-1}. The two peaks at 2923 and 2854 cm^{-1} are due to C−H vibrations of sp^3 carbon. The absence of C−H vibration peaks above 3000 cm^{-1} points out the absence of sp^2-hybridized carbon. The peaks at 1465 and 1378 cm^{-1} are due to C−H bending. The two peaks at 1124 and 1056 cm^{-1} are related to C−O stretching in secondary and primary alcohols, respectively. Finally, the out-of-plane rocking of C−H is visible at 722 cm^{-1}. Since the peak at 1056 is much stronger than that at 1124 cm^{-1} we can deduce that most of PCM is constituted by primary alcohol, whereas minor amounts of secondary alcohols are present in the commercial blend. Based on the FTIR spectrum, the melting temperature (23 °C), and the heat of fusion (≈ 200 J g^{-1}), we can tentatively identify 1-dodecanol as the main component of the present PCM [20]. To our knowledge, no detailed structural information for 1-dodecanol is available in the literature, thus preventing the possibility of quantitative modeling of XRD data. For this reason, we proceeded to an *ab initio* characterization of the pure PCM compound to obtain a basic crystallographic model to be used in the analysis of composite samples. Crystal cell indexing was performed using the DICVOL algorithm [62] in the ReXCell software [63], giving a monoclinic lattice with $a = 28.4690$ Å, $b = 4.1233$ Å, $c = 24.0335$ Å, $\beta = 95.49°$ cell parameters as the only solution, and a corresponding cell volume of 1173 $Å^3$. Space group determination performed employing the strategy by Markvardsen et al. [64] resulted in a P 1 -1 extinction symbol, with a P 1 2/m 1 space group symmetry as the most likely attribution; assuming the whole primary alcohol molecule as the asymmetric unit, this settings corresponds to a four alcohol molecules content per unit cell. Additionally, the average volume-weighted crystallite size of the crystallized PCM phase was estimated to be around 80 nm, again in an isotropic crystallite shape hypothesis,

SEM micrographs of the PP and CB are shown in Fig. 3. The micrographs outline the porous nature of the two biogenic compounds. Both materials contain a large amount of open and interconnected porosity with pore size in the order of 20–200 μm. By comparing the skeletal density measured by He pycnometer ($\rho_s^{CB} = 2.77$ g cm^{-3}; $\rho_s^{PP} = 0.88$ g cm^{-3}) and the geometrical density ($\rho_s^{CB} = 0.351$ g cm^{-3}; $\rho_s^{PP} = 0.132$ g cm^{-3}) it is possible to estimate the amount of open pores, which is between 85% and 90% for both materials. Interestingly, both CB and PP possess a sort of "outer shell" which appears substantially dense (Fig. 3).

To further investigate the pore size distribution of the samples and possibly prove the presence of mesopores, Hg porosimetry was carried out. The results (Fig. 4) confirm that 97% of the cuttlebone porosity is larger than 20 μm, such a result is in perfect agreement with the SEM micrographs. Furthermore, only a very limited amount of mesopores was detected (≈ 1% of the total pore volume is below 50 nm). Unfortunately, pomelo peel resulted compressible during the porosimetry test thus the results are not available. However, some characterization of the micro and mesoporosity of PP is already available in the scientific literature: Wu et al. [65] estimated the total volume of micro and mesopores of PP as 0.166 cm^3 g^{-1} by N_2 physisorption. Considering that the total porosity of PP is about 85% (measured by geometrical method) and the skeletal density is 0.88 g cm^{-3}, one can easily determine that the total pore volume is 6.44 cm^3 g^{-1}. On such bases, only a very limited amount of the PP porosity (< 3% of the pores) is in the micro or meso-range. Hence, we can consider both the materials as macroporous for the purpose of the present work, with substantial negligible effects of smaller pores on the PCM storage capacity.

3.2. Characterization of the composites

Both pomelo peel and cuttlebone were able to absorb a large amount of PCM as shown by weight measures (Figs. 5 and 6) and digital microscope micrographs (Fig. 7). Just after impregnation, the PCM load in the composites was 68.9 ± 2.4 wt% and 84.1 ± 1.0 wt% for CB and PP samples, respectively. Based on density measurements and liquid PCM density (0.83 g cm^{-3}), it is possible to calculate the maximum amount of PCM that can be stored in the porous architectures, equal to 67.4 wt% and 84.2 wt% for CB and PP, respectively. Therefore, the weight gain measured after impregnation is consistent with a complete filling of the open pores by the PCM. The weight gain for CB samples is even slightly larger than the theoretical one and this can be attributed to small differences between the samples or the adsorption of a limited amount of PCM as a thin layer on the external surface of CB samples. The PCM absorption in the biogenic architectures was anyhow always very fast and completed in less than 5 min. This is a key advantage with respect to the most common materials used for shape stabilization of PCMs like graphene oxide, graphene foams, and graphene oxide/carbon nanotubes composites. These materials are also able to

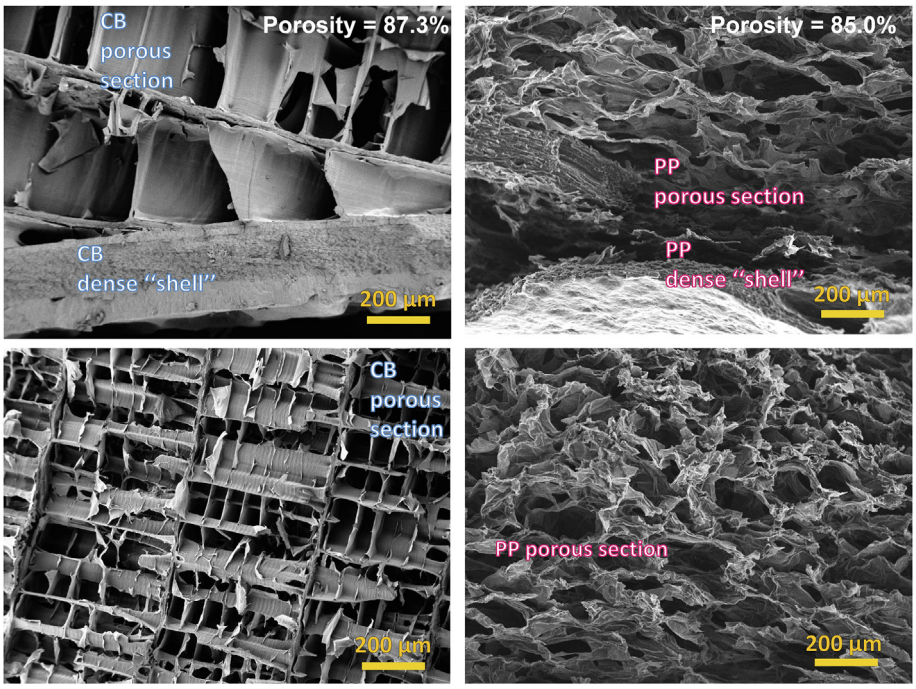

Fig. 3. SEM micrographs of cuttlebone and pomelo peel (not impregnated).

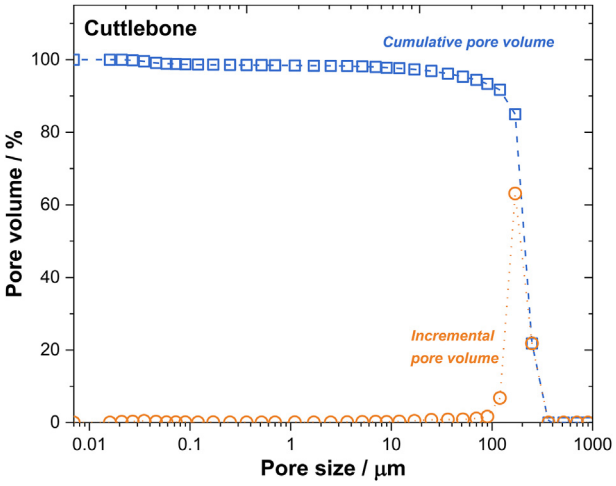

Fig. 4. Cumulative and incremental pore volume distribution as a function of the pore size obtained by Hg porosimetry on cuttlebone.

absorb a huge quantity of PCM (up to 99.5 wt% of paraffin in graphene foams, up to 98.8 wt% in graphene oxide/carbon nanotubes composites, and up to 48.3 wt% of paraffin in graphene oxide) although a very long absorption time is required, 2 h stirring at 90 °C in the case of graphene foam and several hours of vacuum impregnation for graphene oxide [66–68] and graphene oxide/carbon nanotubes composites [67]. Moreover, the PCM absorption ability of PP and CB outperforms that of naturally occurring porous architecture, like diatomite, widely used as shape stabilizers. For instance, TES composites based on diatomite typically contain only 30–60 wt% of PCM [12,15,40–43].

The PCM leakage was investigated on different substrates (earthenware and porphyry bricks, absorbent paper, and aluminum foil) for 14 days after impregnation. The samples were put in contact with the substrates in two different modes: (i) the porous-spongy part of the shape stabilizer touching the substrate (Fig. 5a and b, and Fig. 6a and b); or (ii) localizing the contact on the dense outer shell of the composite matrix (Fig. 5c and d and Fig. 6c and d). When the substrate was in contact with the porous region, the leakage was pretty fast in the case of paper, earthenware, and porphyry. On the other hand, substantially no PCM was released on the aluminum foil. This points out that the capillary pressure in the composites can confine the PCM if the substrate is dense. The leakage kinetics in PP composites are slightly faster than in the case of CB samples.

Interestingly, only a very moderate PCM leakage was detected when the samples laid on their outer shell, regardless of the substrate. After 14 days, the PCM in the composite was ≈ 90% of that measured just after impregnation, the PCM release being almost completely concentrated during the first day (Figs. 5d and 6d). The weight loss in the first days can be likely related to the release of the PCM thin layer adsorbed on the outer surface of the samples. The results point out that CB and PP shells are dense enough to confine the PCM within the porous matrix although the sample is placed on very porous substrates. This is confirmed by the micrographs in Fig. 7, where it is shown that the shape stabilizer porosity is almost completely filled by the PCM in the molten state.

To prove that no substantial chemical interactions take place between the PCM and the shape stabilizer, the composites were investigated by FTIR and XRD (Fig. 8). The spectra recorded on the composites can be fully explained as a superposition of those collected for PCM and the shape stabilizer. Neither new crystalline phases nor new FTIR peaks can be detected, this pointing out that the substrate is substantially inert and does not interact with the PCM. From a powder diffraction perspective, the main difference appears as a reduction in the average crystallite size of the PCM phase when it crystallizes within the shape stabilizer, the other fundamentals crystallographic features remaining substantially the same. In particular, the PCM lattice parameters and corresponding cell volume remain basically unchanged in the composites, further confirming that no significant chemical alteration of the PCM phase takes place. From a microstructural point of view, while the average

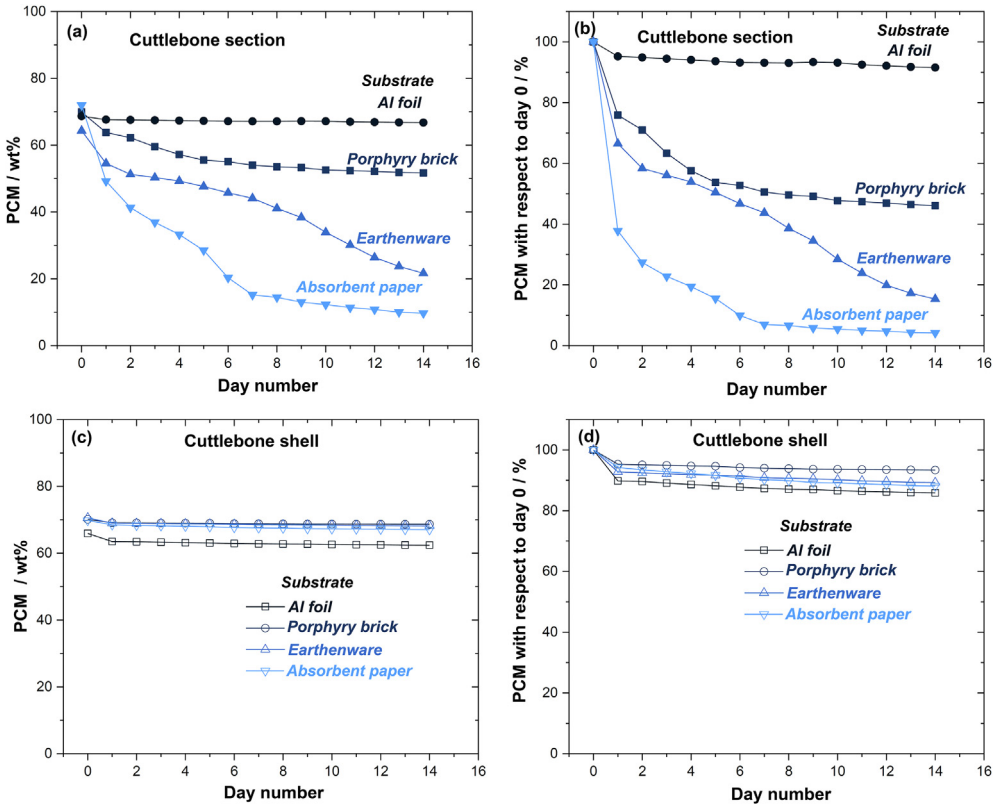

Fig. 5. PCM load in the composites (wt%) and PCM content with respect to the one measured just after impregnation in cuttlebone samples. The PCM leakage is evaluated on different substrates both for samples placed on the substrate on (a,b) their porous region and on (c,d) their outer dense shell.

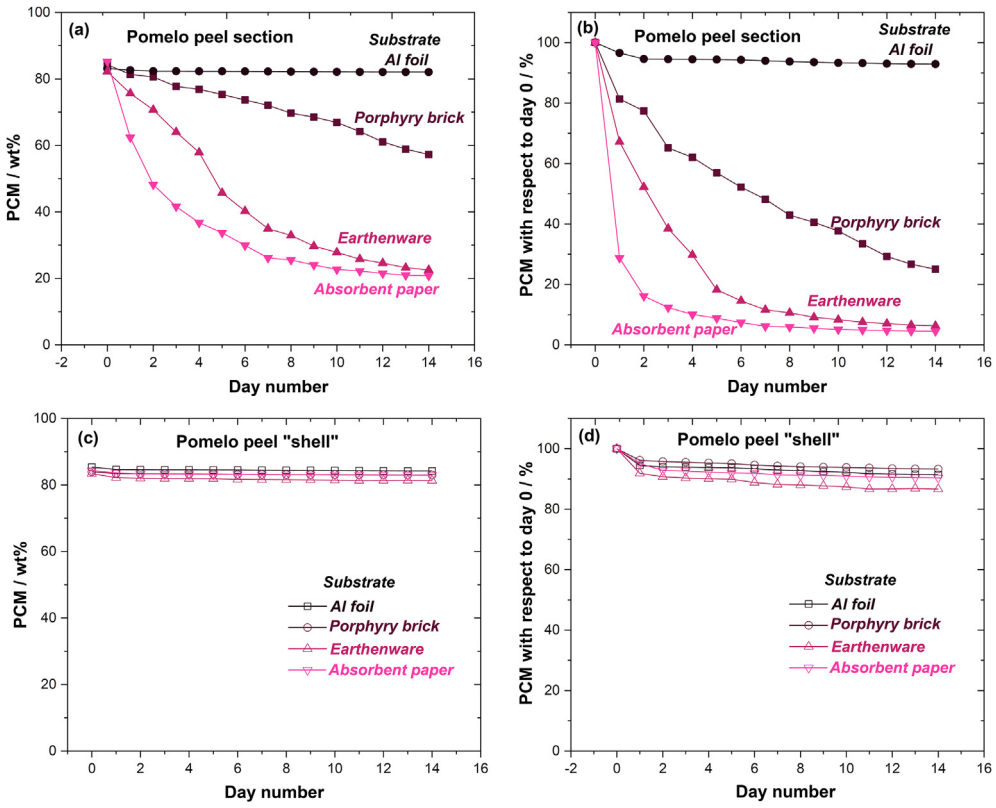

Fig. 6. PCM load in the composites (wt%) and PCM content with respect to the one measured just after impregnation in pomelo peel samples. The PCM leakage is evaluated on different substrates both for samples placed on the substrate on (a,b) their porous region and on (c,d) their outer dense shell.

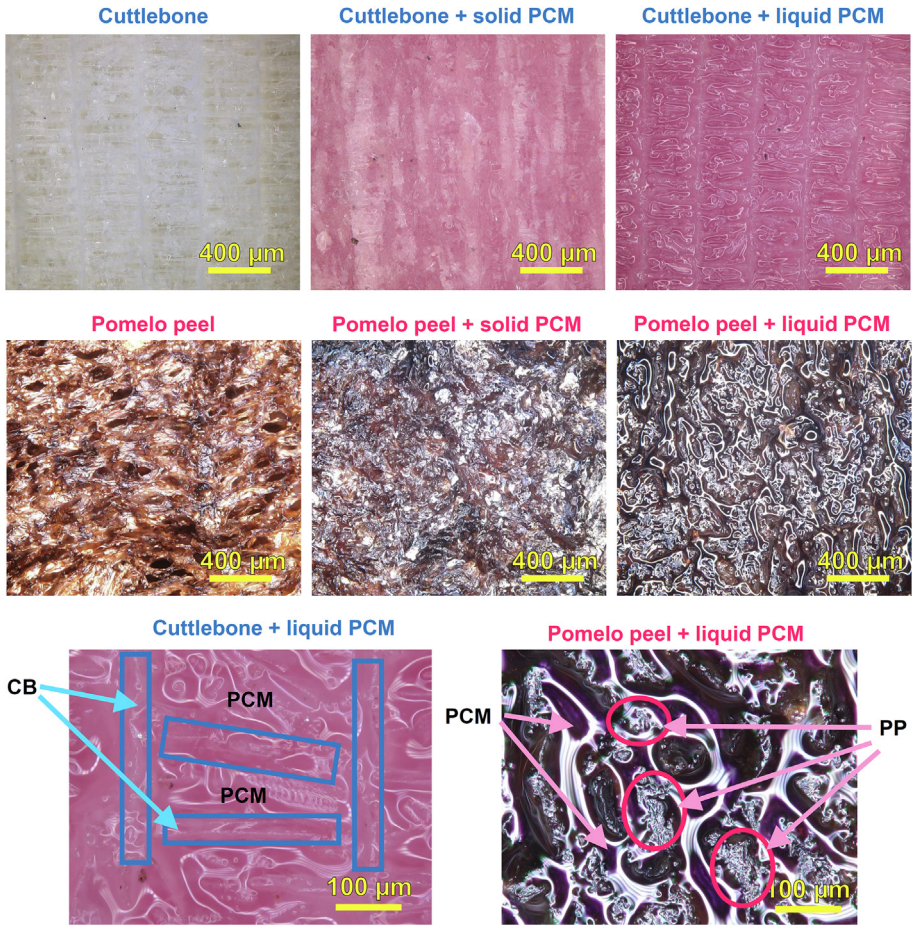

Fig. 7. Digital microscope micrographs of the shape stabilizers (pomelo peel and cuttlebone) and the composites (after the 14-days leakage test) containing the PCM in the solid and liquid phase. The composites are the ones contacting absorbent paper on their dense part during the leakage test. Note that the PCM is pink-colored.

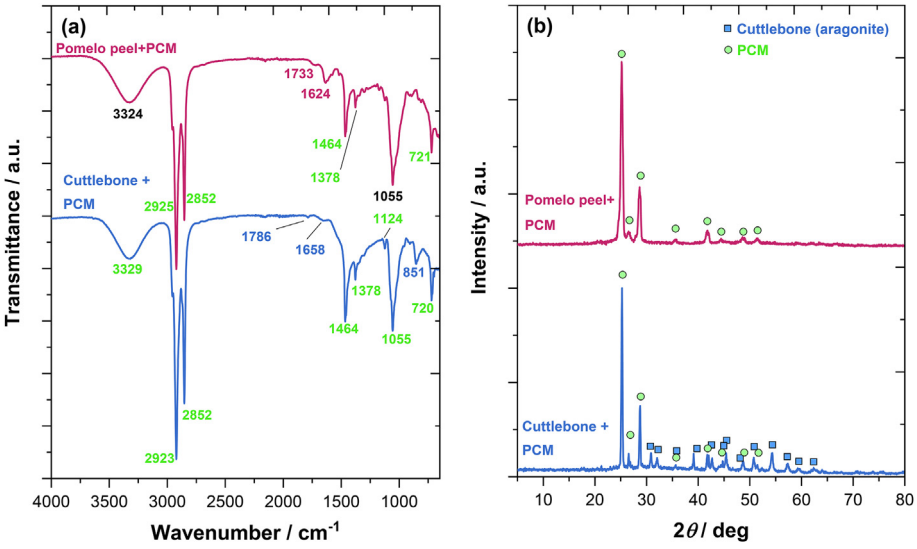

Fig. 8. (a) FTIR spectra of the composites. The peak position label colors identify the typical bands of PCM (green), cuttlebone (blue), and pomelo peel (magenta); black-colored index cannot be attributed to a specific component because of the superposition of different peaks (e.g., the 3324 cm^{-1} band is present both in the PCM and PP). (b) XRD pattern of the composites.

volume-weighted crystallite size of pure PCM is around 80 nm (measured from the spectrum in Fig. 2), it is slightly reduced in the cuttlebone composite (60 nm) and substantially smaller in the PP composite (20 nm). As a secondary effect, it is possible to observe a clear reduction in the diffracted intensity of (0 0 l) basal peaks (located between 10° and 20°) in the composites patterns, likely

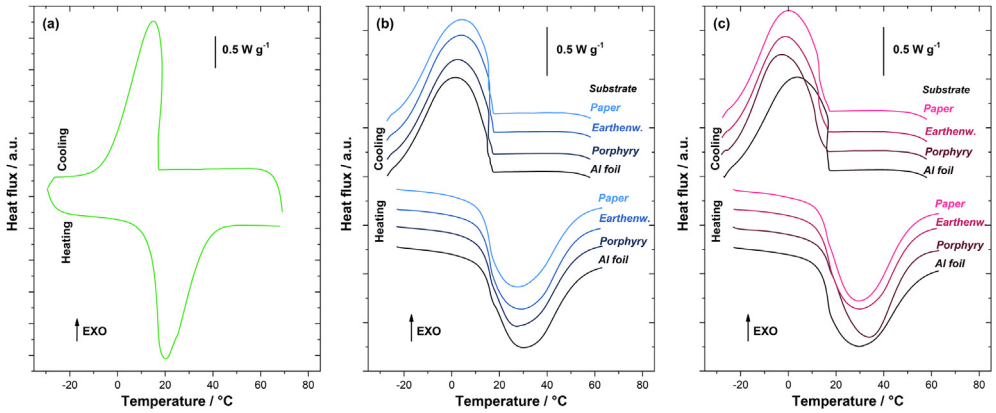

Fig. 9. DSC analysis of (a) the neat PCM, (b) of the CB, and (c) PP composites. The composites were previously subjected to a 14 days PCM leakage test on different substrates (i.e., the tests in Fig. 5 and 6). Only the samples touching the substrate on their outer "shell" were investigated by DSC.

due to isotropic crystal growth and the corresponding absence of preferred orientation features present when the pure PCM is allowed to crystallize free of any physical constraints.

The thermal energy storage capacity of the composites facing the substrates on their "shell" was investigated by DSC after the 14 days leakage test (Fig. 9). Clear endothermic and exothermic peaks due to PCM melting and solidification can be observed in all tested materials regardless of the used substrate. The thermal properties measured by DSC are summarized in Tables 1 and 2. No significant differences in terms of latent heat can be detected upon heating or cooling. One can observe that both composites possess a thermal energy storage capacity close to 145 J g^{-1}, which corresponds to an efficiency of about 70% that of the neat PCM, this value well-matching the PCM load in the cuttlebone composites (Fig. 5). Nevertheless, it appears rather low if compared with the PCM load in the pomelo peel. As a matter of fact, PP composites contain more than 80 wt% PCM at the end of the leakage test (Fig. 6). The reduced efficiency seems unlikely due to small variations in the sample composition as the tests were repeated twice on all the specimens with the same results. Therefore, it seems related to a non-perfect crystallization of the PCM, as shown by the XRD peaks broadening in the PP composite (Fig. 8b). The origin of this effect has not been completely understood so far and could be possibly investigated in future works. Nevertheless, we can suppose that it might be related to the large amount of low-molecular-weight compounds in PP that can migrate and dissolve in the PCM, thus hindering its crystallization.

The volumetric thermal energy storage capacity (i.e., the latent heat normalized to the sample volume) is in the order of 150 J cm^{-3} and 110 J cm^{-3} for CB and PP composites, respectively. The results are quite attractive especially for the CB samples, as their volumetric thermal energy storage is close to 90% of that of the neat PCM.

The efficiency measured in the present work ($\approx$ 70%) is higher than that reached using graphene oxide for shape stabilization ($\approx$ 50%) of a very common PCM (paraffin) but lower than the efficiency obtained by using graphene foams and graphene oxide foams (around 99%) [66–68]. In any case, the lower efficiency shown by the biogenic architecture can be compensated by some other advantages, like the instantaneous absorption of PCM, the fact that both matrix and PCM are derived from natural resources, and that they are biodegradable and cheap.

Looking at the value of the onset melting and crystallization temperatures ($T_{on,m}$ and $T_{on,c}$) it is possible to observe that the values are around 13 °C for all the samples and the difference with the neat PCM is only 2 °C. On the other hand, a clear shift in the composite melting and solidification temperature (T_m and T_c) with respect to neat PCM can be observed (Tables 1 and 2). This can be attributed to the predictable lower thermal conductivity of the

Table 2
Thermal properties measured by DSC (Figs. 8 and 9) upon cooling: onset crystallization temperature ($T_{on,c}$), crystallization peak temperature (T_c); latent heat of crystallization normalized on the sample mass ($\Delta H_{wt,c}$) and volume ($\Delta H_{vol,c}$); thermal energy storage efficiency compared to the pure PCM with respect to the sample mass ($\eta_{wt,c}$) and volume ($\eta_{vol,c}$).

	$T_{on,c}$/°C	T_c/°C	$\Delta H_{wt,c}$/J g^{-1}	$\Delta H_{vol,c}$/J cm^{-3}	$\eta_{wt,c}$/%	$\eta_{vol,c}$/%
CB_earthenware	16.7	3.9	143.8	157.7	70.3	92.4
CB_porphyry	16.0	2.5	144.4	137.0	70.6	80.3
CB_aluminum	16.1	0.5	142.8	161.7	69.8	94.8
CB_paper	16.4	4.2	142.0	151.0	69.4	88.5
PP_earthenware	13.6	−1.1	143.5	99.7	70.2	58.4
PP_porphyry	13.4	−2.7	143.2	118.1	70.0	69.2
PP_aluminum	16.6	0.3	153.3	119.1	75.0	69.8
PP_paper	14.3	0.7	146.3	113.6	71.5	66.6
PCM	17.1	16.0	204.5	169.7	–	–

Table 1
Thermal properties measured by DSC (Fig. 9) upon first heating: onset melting temperature ($T_{on,m}$), melting peak temperature (T_m); latent heat of fusion normalized on the sample mass ($\Delta H_{wt,m}$) and volume ($\Delta H_{vol,m}$); thermal energy storage efficiency compared to the pure PCM with respect to the sample mass ($\eta_{wt,c}$) and volume ($\eta_{vol,c}$).

	$T_{on,m}$/°C	T_m/°C	$\Delta H_{wt,m}$/J g^{-1}	$\Delta H_{vol,m}$/J cm^{-3}	$\eta_{wt,m}$/%	$\eta_{vol,m}$/%
CB_earthenware	13.3	28.5	143.1	157.0	69.6	92.0
CB_porphyry	13.0	27.2	144.2	136.8	70.2	80.2
CB_aluminum	13.1	27.1	142.5	161.4	69.3	94.6
CB_paper	13.2	29.7	142.2	151.2	69.2	88.6
PP_earthenware	13.6	31.8	143.2	99.5	69.7	58.3
PP_porphyry	13.8	33.4	143.7	118.5	69.9	69.5
PP_aluminum	13.1	29.1	153.4	119.1	74.6	69.8
PP_paper	14.3	29.5	146.5	113.7	71.2	66.7
PCM	12.1	19.8	205.6	170.6	–	–

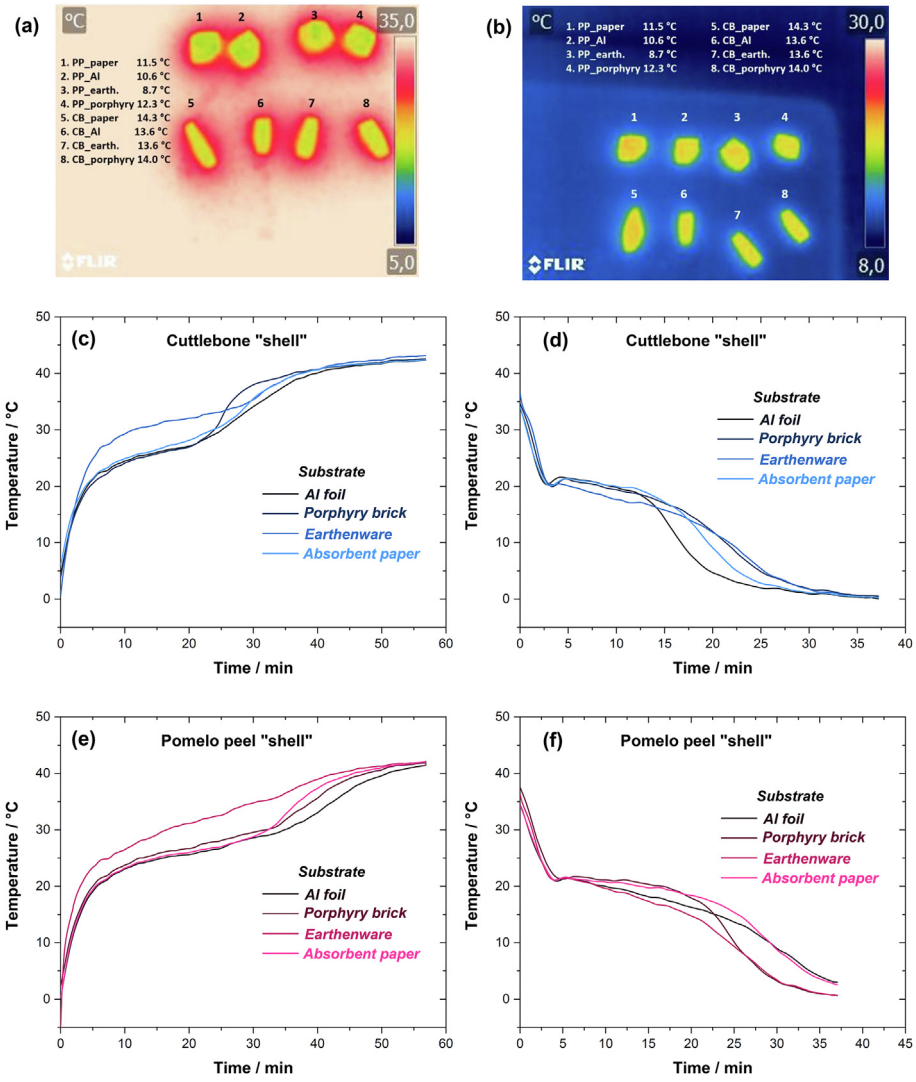

Fig. 10. Thermal camera images of the samples acquired 5 min after the heating (a) and cooling (b) tests had started. Temperature profiles of cuttlebone (c,d) and pomelo peel (e,f) composites: heating stage (left) and cooling stage (right). The composites were previously subjected to a 14 days PCM leakage test on different substrates (i.e., the tests in Fig. 5 and 6). Only the samples touching the substrate on their outer "shell" were tested.

Table 3
Results of the thermal imaging tests on the prepared samples: time to reach a temperature of 3 °C during cooling (t_3) and time to reach a temperature of 40 °C during heating (t_{40}).

Sample	t_3/min	t_{40}/min
CB_earthenware	27.8	35.1
CB_porphyry	27.6	33.2
CB_aluminum	22.5	36.8
CB_paper	24.7	35.1
PP_earthenware	30.4	40.1
PP_porphyry	30.2	44.8
PP_aluminum	36.9	48.4
PP_paper	36.1	43.0

composite. This would certainly be a disadvantage for TES composites to be used in industrial furnaces or solar thermal power stations but it is not necessarily negative when considering applications in buildings. In fact, the time needed to melt (or crystallize) the composite increases with its thermal resistance, thus allowing stabilization of the building temperature for a longer time. The melting (and crystallization) delay appears larger for PP composites, very likely because of the nanocrystalline nature of the shape stabilizer. This result appears consistent with the thermal evolution of the composites shown in Fig. 10 (whose fundamental results are summarized in Table 3). Here, the composites with the PCM in the solid-state were introduced in a furnace at 40 °C, and the thermal evolution was studied using a thermal imaging camera (Fig. 10a,c,e). The successive cooling path is reported in Fig. 10b,d,f and one can observe that in all cases the temperature stabilizes around the melting point of PCM. Nevertheless, the plateau appears definitively longer in the case of PP composites. Looking at the results in Table 3 it is possible to observe that t_3 and t_{40} values (i.e., the time needed to reach 3 °C upon cooling and 40 °C upon heating) are generally larger in PP samples. Since the thermal energy storage capacity of CB and PP samples is substantially the same (Tables 1 and 2), this difference can be likely attributed to the lower thermal conductivity of the PP samples.

The stability of the thermal energy storage properties was verified over 100 melting/solidification cycles after the leakage test on absorbent paper (Fig. 11 and Table 4). One can observe that after 100 cycles the CB_paper sample presents an enthalpy loss of about 0.5% (0.7 J g^{-1}), while the PP_paper sample presents an enthalpy

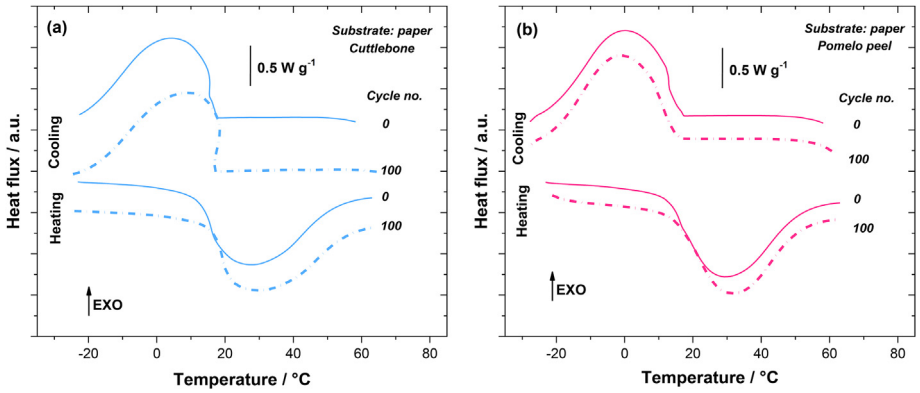

Fig. 11. DSC of (a) the CB and (b) PP composites before and after 100 thermal cyclings (solidification/fusion). The composites were previously subjected to a 14 days PCM leakage test on absorbent paper (i.e., the tests in Fig. 5 and 6). Only the samples touching the substrate on their outer "shell" were investigated by DSC.

Table 4
Thermal properties measured by DSC after 20, 60, 100 cycles: melting peak temperature (T_m); latent heat of fusion normalized on the sample mass ($\Delta H_{wt,m}$), crystallization peak temperature (T_c); latent heat of crystallization normalized on the sample mass ($\Delta H_{wt,c}$).

	Cycle no.	$\Delta H_{wt,m}$/J g^{-1}	$\Delta H_{wt,c}$/J g^{-1}
CB_paper	0	142.2	142.0
	20	142.2	141.9
	60	141.9	141.3
	100	141.5	141.2
PP_paper	0	146.5	146.3
	20	146.5	146.4
	60	143.7	143.0
	100	140.9	140.8

loss of 3.8% (5.6 J g^{-1}). These values, and in particular the ones of the CB sample demonstrate the stability of the prepared samples and their ability to maintain the thermal properties over thermal cycling. The highest thermal stability of the composite based on cuttlebone matrix is likely related to the inorganic nature of the shape stabilizer which ensures no chemical interactions with the PCM. On the other hand, some weak interactions between the PCM and pomelo peel seem possible (see for instance the XRD peak broadening in Fig. 8), thus causing a limited reduction of the thermal properties over cycling.

4. Conclusions

In this work, new environmentally friendly, renewable, and biodegradable thermal energy storage composites were developed. The phase change material, a commercially available agriculture-derived alcohol, was shape-stabilized using porous waste materials, namely cuttlebone and pomelo peel. FTIR and XRD analyses evidenced no significant chemical interactions between the shape stabilizer and the PCM.

The composites show excellent resistance to the leakage of molten PCM (even in contact with porous substrates, such as absorbent paper) thanks to the presence of dense skin surrounding their porous inner structure. After 14 days of leakage on different substrates, the thermal energy storage efficiency for both architectures is in the order of 70% that of the pure PCM. The volumetric thermal energy storage efficiency (i.e., the ratio between the composite and PCM melting enthalpies in J cm^{-3}) is close to 90% and 70% for cuttlebone and pomelo peel composites, respectively. The TES properties do not show significant degradation over the first 100 melting/solidification cycles.

Data availability

Research data are available at https://data.mendeley.com/datasets/6bdcnks224/1.

Funding

This work was supported by the Italian Ministry of University and Research (MIUR) [programs: PRIN2017 - 2017FCFYHK; PRIN2017 - 2017PMR932 and Departments of Excellence 2018–2022] and Provincia Autonoma di Trento (Italy) through Legge 6/99 [project: "Compositi elastomerici a transizione di fase [E-PCM] prat. n. 23-16"].

CRediT authorship contribution statement

Mattia Biesuz: Conceptualization, Methodology, Data curation, Visualization, Writing – original draft. **Francesco Valentini:** Methodology, Investigation, Data curation, Writing – original draft. **Mauro Bortolotti:** Investigation, Data curation, Software. **Andrea Zambotti:** Investigation, Writing – review & editing. **Francesca Cestari:** Investigation, Data curation. **Angela Bruni:** Investigation. **Vincenzo M. Sglavo:** Funding acquisition, Writing – review & editing. **Gian D. Sorarù:** Funding acquisition, Writing – review & editing, Supervision. **Andrea Dorigato:** Funding acquisition, Writing – review & editing. **Alessandro Pegoretti:** Funding acquisition, Writing – review & editing, Supervision.

Declaration of competing interest

The authors declare that they have no known competing financial interests or personal relationships that could have appeared to influence the work reported in this paper.

Acknowledgements

Mr. Livio Zottele is warmly acknowledge for the technical help and support.

References

[1] S. VijayaVenkataRaman, S. Iniyan, R. Goic, A review of climate change, mitigation and adaptation, Renew. Sustain. Energy Rev. 16 (2012) 878–897, https://doi.org/10.1016/j.rser.2011.09.009.
[2] M. Mofijur, T.M.I. Mahlia, A.S. Silitonga, H.C. Ong, M. Silakhori, M.H. Hasan, N. Putra, S.M. Ashrafur Rahman, Phase change materials (PCM) for solar energy usages and storage: an overview, Energies 12 (2019) 1–20, https://doi.org/10.3390/en12163167.

[3] H. Förster, S. Gores, C. Nissen, N. Renders, S. Dael, M. Sporer, T. Mihai, Trends and projections in Europe 2019, Tracking progress towards Europe's climate and energy targets. https://doi.org/10.2800/51114, 2019.
[4] Y. Konuklu, M. Ostry, H.O. Paksoy, P. Charvat, Review on using micro-encapsulated phase change materials (PCM) in building applications, Energy Build. 106 (2015) 134–155, https://doi.org/10.1016/j.enbuild.2015.07.019.
[5] A. de Gracia, L.F. Cabeza, Phase change materials and thermal energy storage for buildings, Energy Build. 103 (2015) 414–419, https://doi.org/10.1016/j.enbuild.2015.06.007.
[6] Y. Cui, J. Xie, J. Liu, S. Pan, Review of phase change materials integrated in building walls for energy saving, Procedia Eng 121 (2015) 763–770, https://doi.org/10.1016/j.proeng.2015.09.027.
[7] H. Lund, P.A. Østergaard, D. Connolly, B.V. Mathiesen, Smart energy and smart energy systems, Energy 137 (2017) 556–565, https://doi.org/10.1016/j.energy.2017.05.123.
[8] K. Pielichowska, K. Pielichowski, Phase change materials for thermal energy storage, Prog. Mater. Sci. 65 (2014) 67–123, https://doi.org/10.1016/j.pmatsci.2014.03.005.
[9] B. He, V. Martin, F. Setterwall, Phase transition temperature ranges and storage density of paraffin wax phase change materials, Energy 29 (2004) 1785–1804, https://doi.org/10.1016/j.energy.2004.03.002.
[10] J. Pereira da Cunha, P. Eames, Thermal energy storage for low and medium temperature applications using phase change materials – a review, Appl. Energy 177 (2016) 227–238, https://doi.org/10.1016/j.apenergy.2016.05.097.
[11] A. Dorigato, G. Fredi, A. Pegoretti, Thermo-mechanical behavior of novel wood laminae-thermoplastic starch biodegradable composites with thermal energy storage/release capability, Front. Mater. 6 (2019) 76, https://doi.org/10.3389/fmats.2019.00076.
[12] M. Li, Z. Wu, H. Kao, Study on preparation and thermal properties of binary fatty acid/diatomite shape-stabilized phase change materials, Sol. Energy Mater. Sol. Cells 95 (2011) 2412–2416, https://doi.org/10.1016/j.solmat.2011.04.017.
[13] R. Wen, X. Zhang, Y. Huang, Z. Yin, Z. Huang, M. Fang, Y. Liu, X. Wu, Preparation and properties of fatty acid eutectics/expanded perlite and expanded vermiculite shape-stabilized materials for thermal energy storage in buildings, Energy Build. 139 (2017) 197–204, https://doi.org/10.1016/j.enbuild.2017.01.025.
[14] L. Cao, Y. Tang, G. Fang, Preparation and properties of shape-stabilized phase change materials based on fatty acid eutectics and cellulose composites for thermal energy storage, Energy 80 (2015) 98–103, https://doi.org/10.1016/j.energy.2014.11.046.
[15] R. Wen, X. Zhang, Z. Huang, M. Fang, Y. Liu, X. Wu, X. Min, W. Gao, S. Huang, Preparation and thermal properties of fatty acid/diatomite form-stable composite phase change material for thermal energy storage, Sol. Energy Mater. Sol. Cells 178 (2018) 273–279, https://doi.org/10.1016/j.solmat.2018.01.032.
[16] Y. Krishna, N. Aslfattahi, R. Saidur, M. Faizal, K.C. Ng, Fatty acid/metal ion composite as thermal energy storage materials, SN Appl. Sci. 2 (2020) 798, https://doi.org/10.1007/s42452-020-2597-3.
[17] K. Kaygusuz, A. Sari, Thermal energy storage performance of fatty acids as a phase change material, energy sources, Part A recover, Util. Environ. Eff. 28 (2006) 105–116, https://doi.org/10.1080/009083190913971.
[18] E.M. Shchukina, M. Graham, Z. Zheng, D.G. Shchukin, Nanoencapsulation of phase change materials for advanced thermal energy storage systems, Chem. Soc. Rev. 47 (2018) 4156–4175, https://doi.org/10.1039/C8CS00099A.
[19] W. Aftab, X. Huang, W. Wu, Z. Liang, A. Mahmood, R. Zou, Nanoconfined phase change materials for thermal energy applications, Energy Environ. Sci. 11 (2018) 1392–1424, https://doi.org/10.1039/C7EE03587J.
[20] L. Feng, S. Dong, H. Zhou, L. Yang, F. Yuan, Y. Yang, J. Lei, L. Bao, L. Bian, J. Wang, n-Dodecanol nanocapsules with supramolecular lock shell layer for thermal energy storage, Chem. Eng. J. 389 (2020) 124483, https://doi.org/10.1016/j.cej.2020.124483.
[21] G. Fredi, A. Dorigato, A. Pegoretti, Novel reactive thermoplastic resin as a matrix for laminates containing phase change microcapsules, Polym. Compos. 40 (2019) 3711–3724, https://doi.org/10.1002/pc.25233.
[22] X. Huang, X. Chen, A. Li, D. Atinafu, H. Gao, W. Dong, G. Wang, Shape-stabilized phase change materials based on porous supports for thermal energy storage applications, Chem. Eng. J. 356 (2019) 641–661, https://doi.org/10.1016/j.cej.2018.09.013.
[23] M.M. Umair, Y. Zhang, K. Iqbal, S. Zhang, B. Tang, Novel strategies and supporting materials applied to shape-stabilize organic phase change materials for thermal energy storage–A review, Appl. Energy 235 (2019) 846–873, https://doi.org/10.1016/j.apenergy.2018.11.017.
[24] G. Fang, F. Tang, L. Cao, Preparation, thermal properties and applications of shape-stabilized thermal energy storage materials, Renew. Sustain. Energy Rev. 40 (2014) 237–259, https://doi.org/10.1016/j.rser.2014.07.179.
[25] G. Fredi, A. Dorigato, L. Fambri, A. Pegoretti, Wax confinement with carbon nanotubes for phase changing epoxy blends, Polymers (Basel) 9 (2017) 405, https://doi.org/10.3390/polym9090405.
[26] F. Valentini, A. Dorigato, A. Pegoretti, Novel EPDM/paraffin foams for thermal energy storage applications, IN PRESS, Rubber Chem. Technol. (2020), https://doi.org/10.5254/rct.21.79976.
[27] Y. Hong, G. Xin-Shi, Preparation of polyethylene-paraffn compound as a form-stable solid-liquid phase change material, Sol. Energy Mater. Sol. Cells 64 (2000) 37–44, https://doi.org/10.1016/S0927-0248(00)00041-6.
[28] I. Krupa, G. Miková, A.S. Luyt, Polypropylene as a potential matrix for the creation of shape stabilized phase change materials, Eur. Polym. J. 43 (2007) 895–907, https://doi.org/10.1016/j.eurpolymj.2006.12.019.
[29] A. Dorigato, D. Rigotti, A. Pegoretti, Thermoplastic polyurethane blends with thermal energy storage/release capability, Front. Mater. 5 (2018) 1–10, https://doi.org/10.3389/fmats.2018.00058.
[30] Q. Cao, P. Liu, Hyperbranched polyurethane as novel solid–solid phase change material for thermal energy storage, Eur. Polym. J. 42 (2006) 2931–2939, https://doi.org/10.1016/j.eurpolymj.2006.07.020.
[31] A. Sarı, C. Alkan, A. Karaipekli, O. Uzun, Poly(ethylene glycol)/poly(methyl methacrylate) blends as novel form-stable phase-change materials for thermal energy storage, J. Appl. Polym. Sci. 116 (2010) 929–933, https://doi.org/10.1002/app.
[32] X. Zhou, H. Xiao, J. Feng, C. Zhang, Y. Jiang, Preparation and thermal properties of paraffin/porous silica ceramic composite, Compos. Sci. Technol. 69 (2009) 1246–1249, https://doi.org/10.1016/j.compscitech.2009.02.030.
[33] Y. Zhang, J. Zhang, X. Li, X. Wu, Preparation of hydrophobic lauric acid/SiO2 shape-stabilized phase change materials for thermal energy storage, J. Energy Storage. 21 (2019) 611–617, https://doi.org/10.1016/j.est.2018.12.022.
[34] Z. Xiangfa, X. Hanning, F. Jian, Z. Changrui, J. Yonggang, Pore structure modification of silica matrix infiltrated with paraffin as phase change material, Chem. Eng. Res. Des. 88 (2010) 1013–1017, https://doi.org/10.1016/j.cherd.2010.01.016.
[35] X. Zhang, Q. Lin, H. Luo, S. Luo, Three-dimensional graphitic hierarchical porous carbon/stearic acid composite as shape-stabilized phase change material for thermal energy storage, Appl. Energy 260 (2020) 114278, https://doi.org/10.1016/j.apenergy.2019.114278.
[36] Z. Zhang, X. Fang, Study on paraffin/expanded graphite composite phase change thermal energy storage material, Energy Convers. Manag. 47 (2006) 303–310, https://doi.org/10.1016/j.enconman.2005.03.004.
[37] X. Meng, H. Zhang, L. Sun, F. Xu, Q. Jiao, Z. Zhao, J. Zhang, H. Zhou, Y. Sawada, Y. Liu, Preparation and thermal properties of fatty acids/CNTs composite as shape-stabilized phase change materials, J. Therm. Anal. Calorim. 111 (2013) 377–384, https://doi.org/10.1007/s10973-012-2349-8.
[38] M. Zhou, T. Lin, F. Huang, Y. Zhong, Z. Wang, Y. Tang, H. Bi, D. Wan, J. Lin, Highly conductive porous graphene/ceramic composites for heat transfer and thermal energy storage, Adv. Funct. Mater. 23 (2013) 2263–2269, https://doi.org/10.1002/adfm.201202638.
[39] A. Sarı, A. Bicer, A. Al-Ahmed, F.A. Al-Sulaiman, M.H. Zahir, S.A. Mohamed, Silica fume/capric acid-palmitic acid composite phase change material doped with CNTs for thermal energy storage, Sol. Energy Mater. Sol. Cells 179 (2018) 353–361, https://doi.org/10.1016/j.solmat.2017.12.036.
[40] A. Sarı, A. Bicer, F.A. Al-Sulaiman, A. Karaipekli, V.V. Tyagi, Diatomite/CNTs/PEG composite PCMs with shape-stabilized and improved thermal conductivity: preparation and thermal energy storage properties, Energy Build. 164 (2018) 166–175, https://doi.org/10.1016/j.enbuild.2018.01.009.
[41] X. Guo, Y. Huang, J. Cao, Performance of a thermal energy storage composite by incorporating diatomite stabilized paraffin as phase change material, Energy Build. 158 (2018) 1257–1265, https://doi.org/10.1016/j.enbuild.2017.11.032.
[42] B. Xu, Z. Li, Paraffin/diatomite composite phase change material incorporated cement-based composite for thermal energy storage, Appl. Energy 105 (2013) 229–237, https://doi.org/10.1016/j.apenergy.2013.01.005.
[43] M. Li, Z. Wu, H. Kao, Study on preparation and thermal properties of binary fatty acid/diatomite shape-stabilized phase change materials, Sol. Energy Mater. Sol. Cells 95 (2011) 2412–2416, https://doi.org/10.1016/j.solmat.2011.04.017.
[44] F. Valentini, A. Dorigato, A. Pegoretti, M. Tomasi, G.D. Sorarù, M. Biesuz, Si3N4 nanofelts/paraffin composites as novel thermal energy storage architecture, J. Mater. Sci. 56 (2021) 1537–1550, https://doi.org/10.1007/s10853-020-05247-5.
[45] P. Tao, D.J. McCaffert, Bioinspired thermal insulation and storage materials, in: T. Deng (Ed.), Bioinspired Eng. Therm. Mater, Wiley, Weinheim (Germany), 2018, pp. 201–223.
[46] A. Sola-Rabada, P. Sahare, G.J. Hickman, M. Vasquez, L.T. Canham, C.C. Perry, V. Agarwal, Biogenic porous silica and silicon sourced from Mexican Giant Horsetail (Equisetum myriochaetum) and their application as supports for enzyme immobilization, Colloids Surf. B Biointerfaces 166 (2018) 195–202, https://doi.org/10.1016/j.colsurfb.2018.02.047.
[47] K. Okada, T. Isobe, K. Katsumata, Y. Kameshima, A. Nakajima, K.J.D. MacKenzie, Porous ceramics mimicking nature—preparation and properties of microstructures with unidirectionally oriented pores, Sci. Technol. Adv. Mater. 12 (2011), 064701, https://doi.org/10.1088/1468-6996/12/6/064701.
[48] Pomelo, n.d, https://www.tridge.com/intelligences/pomelo/production. (Accessed 16 December 2020). accessed.
[49] A.I. Arkhipkin, P.G.K. Rodhouse, G.J. Pierce, W. Sauer, M. Sakai, L. Allcock, J. Arguelles, J.R. Bower, G. Castillo, L. Ceriola, C.-S. Chen, X. Chen, M. Diaz-Santana, N. Downey, A.F. González, J. Granados Amores, C.P. Green, A. Guerra, L.C. Hendrickson, C. Ibáñez, K. Ito, P. Jereb, Y. Kato, O.N. Katugin, M. Kawano, H. Kidokoro, V.V. Kulik, V.V. Laptikhovsky, M.R. Lipinski, B. Liu, L. Mariátegui, W. Marin, A. Medina, K. Miki, K. Miyahara, N. Moltschaniwskyj, H. Moustahfid, J. Nabhitabhata, N. Nanjo, C.M. Nigmatullin, T. Ohtani, G. Pecl, J.A.A. Perez, U. Piatkowski, P. Saikliang, C.A. Salinas-Zavala, M. Steer, Y. Tian, Y. Ueta, D. Vijai, T. Wakabayashi, T. Yamaguchi, C. Yamashiro, N. Yamashita, L.D. Zeidberg, World squid fisheries, Rev. Fish. Sci. Aquac. 23 (2015) 92–252, https://doi.org/10.1080/23308249.2015.1026226.

[50] F.A. Miller, C.H. Wilkins, Infrared spectra and characteristic frequencies of inorganic ions, Anal. Chem. 24 (1952) 1253–1294, https://doi.org/10.1021/ac60068a007.
[51] D. Chakrabarty, S. Mahapatra, Aragonite crystals with unconventional morphologies, J. Mater. Chem. 9 (1999) 2953–2957, https://doi.org/10.1039/a905407c.
[52] E.N. Caspi, B. Pokroy, P.L. Lee, J.P. Quintana, E. Zolotoyabko, On the structure of aragonite, Acta Crystallogr. Sect. B Struct. Sci. 61 (2005) 129–132, https://doi.org/10.1107/S0108768105005240.
[53] X.-L. Yu, Y. He, Optimal ranges of variables for an effective adsorption of lead(II) by the agricultural waste pomelo (Citrus grandis) peels using Doehlert designs, Sci. Rep. 8 (2018) 729, https://doi.org/10.1038/s41598-018-19227-y.
[54] M.-W. Cheong, S.-Q. Liu, J. Yeo, H.-K. Chionh, K. Pramudya, P. Curran, B. Yu, Identification of aroma-active compounds in Malaysian pomelo (citrus grandis (L.) Osbeck) peel by gas chromatography-Olfactometry, J. Essent. Oil Res. 23 (2011) 34–42, https://doi.org/10.1080/10412905.2011.9712279.
[55] F.R. Marín, C. Soler-Rivas, O. Benavente-García, J. Castillo, J.A. Pérez-Alvarez, By-products from different citrus processes as a source of customized functional fibres, Food Chem. 100 (2007) 736–741, https://doi.org/10.1016/j.foodchem.2005.04.040.
[56] R. Huang, M. Cao, H. Guo, W. Qi, R. Su, Z. He, Enhanced ethanol production from pomelo peel waste by integrated hydrothermal treatment, multienzyme formulation, and fed-batch operation, J. Agric. Food Chem. 62 (2014) 4643–4651, https://doi.org/10.1021/jf405172a.
[57] Y. Wandee, D. Uttapap, P. Mischnick, Yield and structural composition of pomelo peel pectins extracted under acidic and alkaline conditions, Food Hydrocolloids 87 (2019) 237–244, https://doi.org/10.1016/j.foodhyd.2018.08.017.
[58] Q. Shao, H. Liu, A. Zhang, Y. Wan, R. Hu, M. Li, Analysis of volatile components extracted from the peels of four different Chinese pomelos using TDS-GC-MS, J. Sci. Food Agric. 94 (2014) 3248–3254, https://doi.org/10.1002/jsfa.6677.
[59] V.-P. Dinh, T.-D.-T. Huynh, H.M. Le, V.-D. Nguyen, V.-A. Dao, N.Q. Hung, L.A. Tuyen, S. Lee, J. Yi, T.D. Nguyen, L.V. Tan, Insight into the adsorption mechanisms of methylene blue and chromium(<scp>iii</scp>) from aqueous solution onto pomelo fruit peel, RSC Adv. 9 (2019) 25847–25860, https://doi.org/10.1039/C9RA04296B.
[60] Y. Liu, A. Liu, S.A. Ibrahim, H. Yang, W. Huang, Isolation and characterization of microcrystalline cellulose from pomelo peel, Int. J. Biol. Macromol. 111 (2018) 717–721, https://doi.org/10.1016/j.ijbiomac.2018.01.098.
[61] G. Williamson, W. Hall, X-ray line broadening from filed aluminium and wolfram, Acta Metall. 1 (1953) 22–31, https://doi.org/10.1016/0001-6160(53)90006-6.
[62] A. Boultif, D. Louër, Powder pattern indexing with the dichotomy method, J. Appl. Crystallogr. 37 (2004) 724–731, https://doi.org/10.1107/S0021889804014876.
[63] M. Bortolotti, I. Lonardelli, ReX. Cell, A user-friendly program for powder diffraction indexing, J. Appl. Crystallogr. 46 (2013) 259–261, https://doi.org/10.1107/S0021889812045025.
[64] A.J. Markvardsen, W.I.F. David, J.C. Johnson, K. Shankland, A probabilistic approach to space-group determination from powder diffraction data, Acta Crystallogr. Sect. A Found. Crystallogr. 57 (2001) 47–54, https://doi.org/10.1107/S0108767300012174.
[65] Y. Wu, L. Cha, Y. Fan, P. Fang, Z. Ming, H. Sha, Activated biochar prepared by pomelo peel using H3PO4 for the adsorption of hexavalent chromium: performance and mechanism, water, air, Soil Pollut 228 (2017) 405, https://doi.org/10.1007/s11270-017-3587-y.
[66] M. Mehrali, S.T. Latibari, M. Mehrali, H.S.C. Metselaar, M. Silakhori, Shape-stabilized phase change materials with high thermal conductivity based on paraffin/graphene oxide composite, Energy Convers. Manag. 67 (2013) 275–282, https://doi.org/10.1016/j.enconman.2012.11.023.
[67] G. Chen, Y. Su, D. Jiang, L. Pan, S. Li, An experimental and numerical investigation on a paraffin wax/graphene oxide/carbon nanotubes composite material for solar thermal storage applications, Appl. Energy 264 (2020) 114786, https://doi.org/10.1016/j.apenergy.2020.114786.
[68] L. Zhang, R. Li, B. Tang, P. Wang, Solar-thermal conversion and thermal energy storage of graphene foam-based composites, Nanoscale 8 (2016) 14600–14607, https://doi.org/10.1039/C6NR03921A.